International Journal of Environmental Sciences
ISSN: 2229-7359
Vol. 11 No. 10s, 2025
https://theaspd.com/index.php

Effect of Mno_2 Phase Structure and The Guest K^+ Ions on the Complete Catalytic Oxidation of Benzene

Mohan Kurra[1], Shireesha Boyapati[1], T Gopi[2]
[1]Department of Pharmaceutical Chemistry, Telangana University, Nizamabad-503322, India.
[2]Department of Chemistry, RGUKT Basar, Mudhole-504107

Abstract
Four different MnO_2 phase structures prepared by hydrothermal method and tested for complete oxidation of benzene and observed their very different activities as in the following order α-MnO_2>δ-MnO_2>γ-MnO_2>β-MnO_2. Further, ion exchange of guest K^+ cations with H^+ ions by acid treatment of α and δ-MnO_2 catalysts significantly enhanced benzene activity. However, for H-α-MnO_2 it is minimum; $T_{90\%}$ decreased from 264 to 261 °C, whereas for H-δ-MnO_2 maximum; $T_{90\%}$ decreased from 268 to 238 °C and maintained good stability. The significant activity of H-δ-MnO_2 due to better diffusion of benzene from 2D interlayer channels due to lack of bigger K^+ cations.
Keywords: *MnO_2; Phase structure; Benzene; complete oxidation; K^+ exchange*

1. INTRODUCTION

Volatile organic compounds (VOCs) are one of the major air pollutants emitted from the transportation and industrial processes; which pollute the atmosphere directly or indirectly as the formation of photochemical smog and ozone formation [1]. Meanwhile, the inhalation of VOCs can cause savior health effects such as headache, respiratory irritation, skin irritation and even cancer for human beings [2, 3]. Among various VOCs, benzene is one of the most abundant aromatic hydrocarbons found in urban atmospheres; due to its carcinogenic and recalcitrant nature it acts as pollutant [4], hence it is highly desirable to remove benzene from the environment. Many technologies such as adsorption, thermal oxidation and catalytic oxidation have been developed for VOCs abatement in the last few decades [5-8]. Among them, catalytic oxidation is proved to be an effective method, due to its lower operating temperature and less harmful reaction products (CO_2 and H_2O) [7].

Many supported and unsupported noble metals (Pt, Pd, Au and Ag) employed for the complete catalytic oxidation of VOCs and showed high activity at low temperatures [9, 10]. However, due to the high cost, sintering nature, and susceptibility of poisoning of noble metals, researchers started to find the alternative economic catalysts. Transition metal (Fe, Cr, Co, Mn, and Cu) oxides are cheaper alternatives to noble metals as catalysts with sufficient activity in the complete catalytic oxidation of VOCs [11–14], though they are less active than noble metals at low temperatures [15]. Among them, MnO_2 is proved to be a one of the promising candidate among the other transition metal oxides for the catalytic oxidation of VOCs due to its distinctive physical and chemical properties, such as multivalent nature and nonstoichiometric composition [2, 16–18]. In recent years, most of the studies have been focused on the relationship between the morphology, phase structure and catalytic activity of MnO_2 catalysts [19–27]. Liang et al., synthesized different MnO_2 phase structures (α, β, γ, and δ) with the same morphology (nanorods) and employed for the CO oxidation [28]. The results showed that the crystal phase and the channel structure of the catalysts played the main role in the activities for CO oxidation and reported high activity on α-MnO_2. In a similar way, Zang et al., reported the effect of different MnO_2 crystal phase structures on formaldehyde oxidation and showed better activity on δ-MnO_2 phase structure [29]. Si et al., prepared various MnO_2 phase structures and examined the effect of phase structure on the complete oxidation of toluene [30]. The γ-MnO_2-SR structure possessed the best activity among the other samples, which was due to the three-dimensional macroporous and mesoporous morphology. It was also reported that, with the variation of selected VOC diameter, the catalytic activity may vary as Genuino et al., reported the order of conversion of few VOCs o-xylene ≈ m-xylene < p-xylene < ethylbenzene < benzene < toluene on OMS-2 at 250 °C [25]. In contrast, Liu et al., reported that the exchange of guest cations like K^+ ions with H^+ ions in the δ-MnO_2 phase structure could increase the adsorption of methyl orange [31]. Whereas, Hou et.al., reported that increase of K^+ concentration lead to a considerable enhancement of the lattice oxygen activity for benzene oxidation on OMS-2 nanorods [4].

Hence, it is important to find an exact MnO_2 phase structure responsible for the complete catalytic oxidation of benzene. Because these structures differ in the MnO_6 octahedra linkages with different

magnitudes in the gaps/tunnels [32]. So, the MnO_2 catalysts with α, β, γ and δ phase structures were prepared by a hydrothermal method and the guest K^+ ions exchanged with H^+ ions in α and δ phases then tested their performance for the complete catalytic oxidation of benzene and explained the probable reasons.

2. Experimental

Preparation of catalysts

The four types of manganese oxide with different phase structures prepared by a hydrothermal method according to the previous report [29]. All the reactants mixed in 80 mL distilled water for about 30 min to form a homogeneous solution and further transferred to a Teflon lined stainless steel autoclave/par reactor (100 mL). After that, the autoclave heated to following temperatures.

For α-MnO_2, 0.525 g $MnSO_4.H_2O$ and 1.25 g $KMnO_4$ reacted at 160 °C for 12 h, for β-MnO_2, 1.69 g $MnSO_4.H_2O$ and 2.28 g $(NH_4)2S_2O_8$ reacted at 140 °C for 12 h, for γ-MnO_2, 3.375 g $MnSO_4.H_2O$ and 4.575 g $(NH_4)2S_2O_8$ reacted at 90 °C for 24 h, and for δ-MnO_2, 0.275 g $MnSO_4.H_2O$, and 1.5 g $KMnO_4$ reacted at 240 °C for 24 h. The final products filtered, washed, dried at 80 °C for 12 hours and then calcined at 300 °C (at a rate of 2 °C/min) for about 3 h.

Ion Exchange. For the preparation of protonated H-α-MnO_2, H-δ-MnO_2, the α, and δ-MnO_2 samples were ion-exchanged (K^+ for H^+) according to the previously reported literature by dispersing the sample (0.5 g) into 1 M HNO_3 at a constant stirring and temperature (70 °C) for 90 min [31, 33]. Further, the ion-exchanged samples thoroughly washed and dried similar to above described procedure.

Characterization of catalysts

The above-prepared catalysts were characterized by XRD, BET surface area, SEM, TPR and XPS analysis. X-ray diffraction (XRD) patterns of calcined catalysts were recorded on an X-ray diffractometer (Shimadzu Corporation) using Ni-filtered Cu Kα radiation (λ= 1.5406 Å) with a scan speed of 2^O per min at a scan range of 10-80^O at 30 KV.

The specific surface areas of the catalysts were measured by a multipoint nitrogen adsorption isotherm at -196 ^{O}C. The nitrogen adsorption-desorption isotherms were obtained on a Micromeritics Instruments surface area analyzer. Prior to this, the catalyst (0.1 g) sample was loaded into a quartz reactor and degassed at 180 ^{O}C for 3 h to desorb the moisture.

The surface morphology of MnO_2 catalysts analyzed with an FEI Quanta 200 scanning electron microscope (SEM) and a high-resolution transmission electron microscope (TEM, JEOL JEM-2100 analyzer). Prior to this, for SEM, the samples coated on the thin carbon tape to avoid charge effect, and the images recorded at a magnification of 10000 and for TEM, a tiny amount of catalyst was dispersed in ethanol by sonication and a drop of sample was placed on a carbon-coated copper grid, further it was dried in a hot oven for 30 min and analyzed by HR-TEM.

The extent of reducibility of catalyst was measured by H_2-temperature programmed reduction (H_2-TPR) on a TPR unit (Nuchrom Technologies) equipped with a thermal conductivity detector (TCD). The 5.6 % H_2 in argon mixture was passed through a catalyst (0.1 g) at a flow rate of 50 mL/min while increasing the temperature from 40 to 600 °C at a rate of heating 10 °C/min.

The oxygen evolution of prepared catalysts was measured by O_2-temerature programmed desorption (O_2-TPD) on a TPD unit (Nuchrom Technologies) equipped with a TCD. The ultra-pure He was passed through a catalyst (0.1 g) at a flow rate of 50 mL/min while increasing the temperature from 50 to 720 °C at a rate of heating 10 °C/min. The outlet of reactor passed through an isopropanol slurry to trap the moisture.

The surface atom properties were measured at room temperature with an X-ray photoelectron spectroscopy (XPS, Oxford Instruments) with an Al anode for K_α (hν = 1486.7 eV) radiation. The binding energy values were calibrated by using the C1s peak (284.8 eV).

Activity studies

Activity experiments carried out in a continuous flow, fixed-bed quartz reactor at an atmospheric pressure. The 100 mg of catalyst diluted with 250 mg of quartz beads and loaded between two quartz wool plugs in a reactor and mounted vertically in an electrically heated tubular furnace (Carbolite, USA). Further, the catalyst temperature raised to 100 °C at a rate of 5 °C/min and kept for 1 hour to remove the species any adsorbed on the surface of the catalyst. Further, the reaction mixture (720 ppmv benzene) was introduced at a gas hourly space velocity of 30000 h^{-1} g^{-1}_{cat} and measured the activity in the temperature range of 100 to 270 °C. The reactant benzene (Aldrich, 99.9%) was injected by a precise infusion pump (KD Scientific, 2000) into the preheating chamber and the atmospheric compressed dry air was used as

carrier and oxidant. All the gas streams were preheated at 90 °C, before entering into the reactor to minimize the condensation of reactants and the flow rate (50 mL/min) was maintained by a precise mass flow controller (Sierra Instruments Inc, flow accuracy ±1 %).

The quantitative product analysis was done by passing the gas stream into an Online GC equipped with FID detector (Bruker GC) using an HP-5 capillary column (30 m x 0.25mm) whereas, the qualitative analysis was done by GC-MS (Agilent 6890N) using DB-5 capillary column (30 m x 0.25 mm). Volatile compounds were analyzed with CO (Technovation Analytical Instruments Ltd., SR 94, range 1-2000 ppmv), and CO_2 (Technovation Analytical Instruments Ltd., P90, range 10-20000 ppmv) analyzers, respectively.

% conversions were measured by the following equation:

$$\% \text{ conversion} = \frac{C_{in} - C_{out}}{C_{in}} \times 100 \quad (1)$$

C_{in} = concentration of benzene in absence of catalyst and C_{out} = concentration of benzene during the reaction.

3. RESULTS AND DISCUSSION

XRD and BET-SA studies

From the XRD results (Figure.1), the lattice constants of prepared catalysts are in good agreement with the respective phase structures. The XRD pattern of α-MnO_2 is well indexed to a cryptomelane-type manganese oxide (JCPDS 44-0141), whereas, the XRD patterns of β-MnO_2 and γ-MnO_2 are in good agreement with pyrolusite-type (JCPDS 24-0735) and nsutite-type (JCPDS 14-0644) manganese oxides, respectively. On the other hand, the XRD pattern of δ-MnO_2 is characteristic of a birnessite-type manganese oxide with a layered structure (JCPDS 80-1098). The XRD patterns indicate that the prepared catalysts are well crystallized with no other impurity phases. The structural variations in the XRD patterns of manganese oxides due to the different bonding ways of the basic MnO_6 octahedral units [28]. The ways in which the corners and edges of the MnO_6 octahedral units are combined are important in terms of the tunnel structure; the tunnel size, based on the number of octahedral subunits (n × m), can be used to define different crystallographic forms (Figure 2) [28, 34], α-MnO_2 consists of double chains of edge-sharing MnO_6 octahedra, which are linked at corners to form (2 × 2) and (1 × 1) tunnels that extend in a direction parallel to the c-axis of the tetragonal unit cell. The sizes of the (2 × 2) and (1 × 1) tunnels are ~4.6 and ~1.89 Å, respectively and the (2 × 2) tunnel occupied by K^+ ions resulted from the preparation method [32]. The single chain of β-MnO_2 is linked with the adjacent chains through common corners of the MnO_6 octahedra, resulting in (1 × 1) tunnels [35]. The crystal structure of γ-MnO_2 consists of a random intergrowth of ramsdellite ((2 × 1) tunnels, ~2.3 Å) and pyrolusite ((1 × 1) tunnels) structures, with clear stacking faults [34, 36]. In contrast, δ-MnO_2 forms a 2D layer structure and it is theoretically built up from layers of edge sharing MnO_6 octahedra, and the spacing between the layers is ~7 Å and these layers may occupy by K^+ ions [37].

From the BET surface area results (Table 1.), the δ-MnO_2 possesses higher surface area (164 m^2/g) and pore volume (0.42 cm^3/g) among all other catalysts and the order of surface area and pore volume is β-MnO_2 < γ-MnO_2 < α-MnO_2 < δ-MnO_2. The difference in the surface area and pore volumes might be due to the difference in the crystal structures and the size of the MnO_2 particles. The lowest surface area of β-MnO_2 could be due to its smallest tunnel size (1 x 1) resulted from the densely packed MnO_6 octahedra [30]. Conversely, the high surface area of α-MnO_2 and δ-MnO_2 might be due to their larger channel crystal dimensions (2 x 2 tunnel and layered) than that of β-MnO_2 [30]. The γ-MnO_2 catalyst shown much similar moderate surface area and pore volume, which is related to its moderate tunnel size (2 x 1). The corresponding N_2 adsorption isotherm patterns and pore size distributions of MnO_2 catalysts is displayed in **Figure s1** of supporting information and isotherms represent mesoporous nature.

Surface morphology studies

The surface morphology of synthesized MnO_2 catalysts observed by SEM and TEM techniques and the images are depicted in Figure 3. Figure 3.a.1 – 3.a.3 shows that α-MnO_2 presents as nanorod like structure with a wide range of dimensions; the length of the nanorods measured from SEM images as 0.5 to 3 μm, whereas the diameter from TEM is ranged from 50 to 150 nm. Figure 3.a.4 shows the corresponding high-resolution TEM image and selected area electron diffraction pattern of single nanorod and the fringe distance of 0.492 nm attributed to the lattice spacing of (2 0 0) plane. On the other hand, β-MnO_2 consist (Figure 3.b.1 – 3.b.3) of many fine nanofibers accumulated together to form bowls of several μm in

diameter and the diameter and length of the nanofibers from TEM and SEM ranged from 20 to 100 nm and 0.2 to 1 μm, respectively. Figure 3.b.4 presents the high-resolution TEM image with a fringe distance of 0.320 nm, attributed to the lattice spacing of (1 1 0) plane and correspond electron diffraction pattern. Similarly, Figure 3.c.1 – 3.c.3 and Figure 3.d.1 – 3.d.3 shows γ- and δ-MnO_2 catalysts with spherical nanostructures of several μm in diameter, respectively. The diameter of spherical nanostructure of γ-MnO_2 is about 3 to 5 μm (Figure 3.c.1) and it is composed by MnO_2 nanofibers with sharp tips, like a sea urchin-like cluster and the diameter of these nanofibers are in the range of 5 to 50 nm (Figure 3.c.2 – 3.c.3). Figure 3.c.4 represents high-resolution TEM image and selected area electron diffraction pattern of γ-MnO_2 and correspond fringe distance of 0.402 nm attributed to the lattice spacing of (1 2 0) plane [32]. Whereas, the δ-MnO_2 spherical morphology is built by many interleaving nanoflakes (like a curling lamellar structure), which are grown from the root of the sphere and the gap between the nanoflakes at the top of the sphere is in the range of 50 to 100 nm. The size of the δ-MnO_2 spheres are in the range of 0.3 to 0.8 μm (Figure 3.d.1 – 3.d.3) and these spheres are looked to be highly aggregated. Overall, it appears that all the four MnO_2 catalysts are shown nanostructures with various morphologies.

Temperature programmed studies

The reducibility of MnO_2 catalysts was examined by using H_2-TPR experiments and the results displayed in Figure 4. From the results, two distinctive reduction peaks are observed for β and γ-MnO_2 catalysts. The β-MnO_2 catalyst shown a first reduction peak centered at 372 °C, and the second broad peak at 495 °C. The reduction pattern of γ-MnO_2 is similar to β-MnO_2, but the peak position shifted to little higher temperature, shown at 393 and 555 °C, respectively. The lower temperature peak attributed to the reduction of MnO_2 to Mn_3O_4, whereas the higher temperature peak ascribed to the reduction of Mn_3O_4 to MnO [37]. On the other hand, the α and δ-MnO_2 catalysts shown similar H_2 consumption peaks in the temperature region of 250 to 400 °C and which are very different from the β- and γ-MnO_2. The α and δ-MnO_2 exhibited two overlapped reduction peaks in a narrow temperature range of 300 to 400 °C, with a T_{max} of 372 and 355 °C, respectively, which may attributed to the reduction of MnO_2 to MnO with Mn_2O_3 and Mn_3O_4 as the intermediates [28, 29]. Because, the final green color product, which was observed in the H_2-TPR experiment might be due to the formation of MnO. These results indicate that the reducibility of the four catalysts is in the order of γ < β < α < δ-MnO_2.

The O_2-TPD experiments were performed to investigate the evolution of oxygen from the prepared MnO_2 catalysts (Figure 5). The desorption peak below 350 °C can be ascribed to the release of chemisorbed oxygen, while the peak in the range of 400–650 °C is attributed to the release of sub-surface lattice oxygen and phase transformation from MnO_2 to Mn_2O_3 [38-40]. From the results, the absence of low temperature peak (below 350 °C) on all the catalysts represent the lack of chemisorbed oxygen, which can be due to the prior calcination at 300 °C. In contrast, the presence of high temperature peak on β- and γ-MnO_2 ascribed to desorption of sub-surface lattice oxygen by phase transformation from MnO_2 to Mn_2O_3 [41]. Whereas, the relatively less intense high temperature peak over α-MnO_2 and δ-MnO_2 indicate that the K ions present in the (2 × 2) tunnels and interlayers of 2D structures, respectively might be stabilized the phase structure. Zhao et al., was reported similar observations and are in line with the results [37].

Surface atom properties

In order to identify the surface atom properties, the MnO_2 catalysts are analyzed by XPS analysis and the results are shown in Figure 6.a. The Mn $2p_{3/2}$ XPS peaks are de-convoluted into two peaks with binding energy at 641.6, and 642.8 are ascribed to the Mn^{3+}, and Mn^{4+}, respectively [42]. A quantitative analysis on the molar ratios of surface Mn^{4+}/Mn^{3+} is summarized in Table 1.

The average oxidation state (AOS) of the MnO_2 catalysts is estimated from Mn 3s spectra by using the following formula: AOS = 8.956 - 1.126 x ΔEs, where ΔEs is the binding energy difference between the doublet Mn 3s peaks and the results shown in Table.1 [43]. Because the Mn 3s XPS is more sensitive to the oxidation state of manganese than that of Mn 2p [44]. From the results (Figure s2 in supporting information), the energy differences (E_{3s}) between the main peak and its satellite in the corresponding Mn 3s spectra of α-, β-, γ-, and δ-MnO_2 are 4.57, 4.42, 4.67 and 4.49 eV and their AOS are 3.8, 3.97, 3.69 and 3.9, respectively.

The O 1s XPS of MnO_2 catalysts are shown in Figure 6.b. The asymmetrical O 1s spectra could be de-convoluted into two peaks and a peak at 529 eV is assigned to the lattice oxygen (O_2^-) (denoted as O_{latt}) [30], and the peak at 531.6 eV corresponds to the surface adsorbed oxygen with low coordination (denoted as O_{ads}/mobile oxygen) [45], such as O_2^{2-} or O^- belong to defect-oxide or hydroxyl-like groups.

The surface element molar ratios of O_{latt}/O_{ads} are calculated and summarized in Table 1. From the results, the order of O_{latt}/O_{ads} for MnO_2 catalysts is δ-MnO_2 > β-MnO_2 > α-MnO_2 > γ-MnO_2.

4. Activity studies

The complete catalytic oxidation of benzene as a function of temperature (from 120 to 300 °C, Figure 7.a) studied over α-, β-, γ- and δ-MnO_2 catalysts at a GHSV of 30000 mL/g_{cat}.h with an inlet benzene concentration of 720 ppmv. Further the reaction temperature decreased to 270 °C and continued the reaction for about 240 min to find the stability of catalyst (Figure.7b). From the Figure.7a, though the initial activity of all the catalysts observed at 140 °C, the complete conversion of benzene into CO_2 observed at 180 °C. Further, the benzene conversion values increased with the increase of temperature with a distinct relation. Among them, α-MnO_2 catalyst exhibited better catalytic activity with $T_{50\%}$ and $T_{90\%}$ of 227 and 264 °C, while the other catalysts (β-, γ- and δ-MnO_2) catalysts showed comparatively less catalytic activity than α-MnO_2 and the order is δ-MnO_2 > γ-MnO_2 > β-MnO_2. From the Figure.7b, the benzene conversion with time on stream showed the stable activity for all the MnO_2 catalysts about 240 min. The high stability might be attributed to the hydrophobic nature of MnO_2 catalysts because the good hydrophobicity could prevent the adsorption of water produced from benzene combustion on the active sites [46]. However, the change in the benzene oxidation conversion values over MnO_2 catalysts might be due to the change in the specific surface area, reducibility, surface properties and tunnel (phase) structures.

It is well known that the high surface area could provide the better adsorption on the surface of the catalysts that leads to the better conversions [47]. Comparing the surface areas of MnO_2 catalysts with the results of benzene conversion, it might find that the surface areas have a considerable effect on the catalytic activity. The high surface α and δ-MnO_2 catalysts showed high activity, whereas the moderate and lowest surface γ-MnO_2 and β-MnO_2 showed moderate and lowest catalytic activity, respectively. In addition, the high oxygen mobility causes more oxygen to be adsorbed and further excited to active oxygen, which would then be involved in the reaction [48]. The oxygen mobility in the samples could measure by H_2-TPR reducibility studies; that is the catalyst have high reducibility possess the most mobile oxygen species both at the surface and in the bulk [29]. It is clear from the H_2-TPR reducibility studies α and δ-MnO_2 catalysts have high reducibility than that of γ-MnO_2 and β-MnO_2 catalysts. Hence, α and δ-MnO_2 catalysts may show high conversion values for benzene oxidation. Furthermore, the conversion values and assumptions drowned from TPR studies are correlated with the state of surface elements (Mn and O), which were analyzed by XPS analysis. Wang et al., reported that the adsorbed oxygen species might play an important role in the total oxidation of toluene over MnO_2 catalysts [7]. Whereas, Zhang et al., claimed that the lattice oxygen species could play the major role in the formaldehyde oxidation over MnO_2 catalysts [29]. In an another study, Liang et al., suggested same as Zhang et al., that the surface lattice oxygen rich α and δ-MnO_2 catalysts showed better CO oxidation than that of γ-MnO_2 and β-MnO_2 catalysts [28]. In this study, the benzene oxidation also closely related to the surface concentration of O_{latt} species; that is the high O_{latt}/O_{ads} molar ratio contain α and δ-MnO_2 catalysts showed better benzene conversions, while the low O_{latt}/O_{ads} molar ratio contain γ-MnO_2 exhibited comparatively less benzene conversions. On the other hand, β-MnO_2 catalyst though it has relatively good surface O_{latt}/O_{ads} molar ratio, it showed lowest benzene conversions, which might be due to its small tunnel structure.

MnO_2 tunnel (phase) structure and the activity relationship

As we discussed earlier, the MnO_2 catalysts present the distinct tunnel diameters (Table.1) due to the combination of MnO_6 octahedra in various directions. α-MnO_2 contains (2 × 2) and (1 × 1) tunnel structures, β-MnO2 composed of a (1 × 1) tunnel structure, γ-MnO_2 consists both (1 × 1) and (1 × 2) tunnels. In contrast, δ-MnO2 forms a 2D layer structure. Hence, the activity may vary with the tunnel structure. Saputra et al., stated that the effect of MnO_2 tunnel structure can influence on the phenol adsorption, therefore it clearly affects the catalytic activity of MnO_2 for phenol degradation [49]. In addition, Si et al., reported better toluene oxidation conversion values on α-MnO_2 (2 × 2) tunnel structure among α, β and δ-MnO_2 catalysts [30]. Furthermore, Zhang et al., reported δ-MnO_2 2D layer structure more suitable for the formaldehyde diffusion than the (2 × 2), (1 × 1) and (2 × 1) tunnel structures of α, β, and γ-MnO_2 catalysts, respectively [29]. Whereas, Chen et al., noticed that MnO_2 with the (2 × 2) tunnel structure is more active than the (1 × 1) or (3 × 3) structures for HCHO oxidation since the effective diameter of the (2 × 2) tunnel is more suitable for the HCHO oxidation [44]. In the present study, the benzene oxidation results are closely related to the tunnel structure/diameter; that is α and δ-MnO_2

catalysts with high tunnel diameter (4.6 and 7.0 Å) exhibited better activity than that of β and γ-MnO_2 catalysts with less tunnel diameter (1.89 and 2.30 Å). It is known that benzene diameter is close to 5.8 Å and due to small tunnel diameter of β-MnO_2, benzene molecule may not enter the tunnels, hence the catalytic reaction occurred on the external surface of MnO_2 catalysts [50]. It indicated that the internal surface of the tunnel could not be utilized well, which might be another reason for the low activity of MnO_2 catalysts having small tunnel diameters. In contrast, though, the δ-MnO_2 catalyst have accessible diameter than that of α-MnO_2 catalyst, it is showed lower benzene conversion values.

Effect of guest K^+ ion concentration on the activity of α and δ-MnO_2 catalysts.

As per the earlier reports, the guest K^+ ions presented in the tunnels of α and δ-MnO_2 catalysts may also play the major role on the adsorption of target molecules and finally effect the conversion values [31]. Hence, it is an important parameter to analyze the activity of benzene oxidation on before and after replacement of K^+ ions from the tunnels of α and δ-MnO_2 catalysts. From the EDS results (Table.2 and Figure s3 in supporting information), around 90 % K^+ ions are effectively leached out from the surface by the acid treatment in the δ-MnO_2 catalyst, whereas for the α-MnO_2 catalyst, around 40 to 50 % K^+ ions are leached out. The reason might be the tunnel diameter, due to the smaller diameter (4.6 Å) of (2 × 2) tunnel the K^+ ions presented in the tunnel may not leach out easily, whereas for δ-MnO_2 catalyst due to relatively larger 2D interlayer diameter (7 Å), the K^+ ions are easily leach out. However, the effective crystal structures (Figure 8.a) and morphology (Figure 9) of both the catalysts are unchanged. From the activity results (Table.2), the change in the benzene activity from α-MnO_2 to H-α-MnO_2 slightly increased; that is $T_{50\%}$ decreased from 227 to 225 °C ($\Delta T_{50\%}$= 2 °C) and $T_{90\%}$ decreased from 264 to 261 °C ($\Delta T_{90\%}$= 3 °C). In the case of δ-MnO_2 to H-δ-MnO_2 the benzene activity extremely increased and maintained the good stability (Figure 10); that is $T_{50\%}$ decreased from 232 to 200 °C ($\Delta T_{50\%}$= 32 °C) and $T_{90\%}$ decreased from 268 to 238 °C ($\Delta T_{90\%}$= 30 °C). Liu et al., observed similar results as the replacement of K^+ with H^+ in δ-MnO_2 catalyst considerably increased the adsorption of methyl orange from aqueous solutions [31]. In another study, Sun et al., reported better catalytic combustion activity of diethyl ether and toluene for acid treated OMS-2 catalyst than that of alkali treated and simple OMS-2 catalysts [51]. The superior activity of the acid-treated OMS-2 could be ascribed to the richer surface oxygen, higher oxygen mobility and redox properties.

From the results, it can clearly say that the effect of guest K^+ ions on the benzene activity is minimum for α-MnO_2 whereas for δ-MnO_2 it is maximum. The significant increase in the benzene activity from δ-MnO_2 to H-δ-MnO_2 might be due to the better adsorption or diffusion of benzene from the 2D inter layer channels, increased surface area, reducibility and mobile oxygen. It can observe from Figure 8.b that the decrease of reduction temperature in H_2-TPR experiment from δ-MnO_2 to H-δ-MnO_2 catalyst, which could be due to the high mobile oxygen on the both at the surface and in the bulk. Figure s4 from supporting information shows O1s XPS pattern of δ-MnO_2 and H-δ-MnO_2 catalysts, where it can observe that the increase of O_{ads} peak area from the δ-MnO_2 to H-δ-MnO_2 catalyst. This can be due to the increase of mobile oxygen and as the mobile oxygen increases on the surface of catalyst the activity of oxidation reaction may increase. The similar activity results was observed for ozone decomposition for H-δ-MnO_2 catalyst in our previous study, which might be attributed to surface oxygen vacancies [52]. In this respect, it can say that the K^+ cations in the layered δ-MnO_2 structure have an unfavorable influence on the adsorption or diffusion of benzene onto the δ-MnO_2 catalyst.

The replacement of K^+ ions with H^+ ions significantly increased the activity of both catalysts due to increased pore availability for the adsorption of benzene, which in turn enhances its oxidation. TEM and EDS (Energy Dispersive Spectroscopy) data also suggest that most of the K^+ ions were successfully replaced by H^+ ions (Figure 11(a,b)).

Overall, the surface area, reducibility, mobile oxygen and tunnel structure played an important role in the benzene oxidation on MnO_2 catalysts and distinguished the activity from one phase to the other. Among them, α-MnO_2 phase structure exhibited better activity than that of other phases but after replacement of guest K^+ ions from δ-MnO_2 phase structure, the activity considerably increased and turned to be a better catalyst for the complete oxidation of benzene. These findings prove that H-δ-MnO_2 catalyst is a good alternative for the complete oxidation benzene.

5. CONCLUSION

The four different phase structures α, β, γ and δ-MnO_2 are prepared by hydrothermal method and analyzed with various techniques such as XRD, BET-SA, SEM, TEM, H_2-TPR, O_2-TPD and XPS. Further,

the prepared catalysts are tested for the complete oxidation of benzene and observed their very different activities as in the following order α-MnO_2 > δ-MnO_2 > γ-MnO_2 > β-MnO_2. The significant difference in activities over MnO_2 catalysts are ascribed to their different tunnel structures, surface area, reducibility, and surface mobile oxygen. The better surface area, reducibility and accessible tunnel diameter of α and δ-MnO_2 catalysts increased activity for complete oxidation of benzene than β and γ-MnO_2 catalysts. Among α and δ-MnO_2 catalysts, though α-MnO_2 has less (4.6 Å) tunnel diameter than that of δ-MnO_2 (7 Å) exhibited better conversions, which could be due to the high mobile oxygen of α-MnO_2.

Further, guest K^+ cations of α and δ-MnO_2 catalysts are exchanged with H^+ ions by acid treatment and tested their activities. The activity results showed that the effect of guest K^+ ions on the benzene activity is minimum for α-MnO_2 whereas for δ-MnO_2 it is maximum. The significant increase in the benzene activity from δ-MnO_2 to H-δ-MnO_2 might be due to the better adsorption or diffusion of benzene from the 2D inter layer channels, increased surface area, reducibility and mobile oxygen. These findings prove that H-δ-MnO_2 catalyst is a good alternative for the complete oxidation benzene in the practical applications.

Acknowledgements

REFERENCES

[1] Z. Zhang,, Z. Jiang,, W. Shangguan, Catal. Today 264 (2016) 270–278.
[2] W. Tang,, Y. Deng,, W. Li,, J. Li,, G. Liu,, S. Li,, X. Wu,, Y. Chen, Catal. Sci. Technol. 6(6) (2016) 1710–17108.
[3] T. Gopi,, G. Swetha,, S.C. Shekar,, R. Krishna,, C. Ramakrishna,, B. Saini,, P.V.L. Rao, Arab. J. Chem. (2016).
[4] J. Hou,, L. Liu,, Y. Li,, M. Mao,, H. Lv,, X. Zhao, Environ. Sci. Technol. 47(23) (2013) 13730-13736.
[5] K.J. Kim,, H.G. Ahn, Microporous Mesoporous Mater. 152 (2012) 78–83.
[6] G. Swetha,, T. Gopi,, S. Chandra Shekar,, C. Ramakrishna,, B. Saini,, P.V.L. Rao, Chem. Eng. Res. Des. 117 (2016) 725–732.
[7] F. Wang,, H. Dai,, J. Deng,, G. Bai,, K. Ji,, Y. Liu, Environ. Sci. Technol. 46(7) (2012) 4034–4041.
[8] C. Ramakrishna,, R. Krishna,, T. Gopi,, G. Swetha,, B. Saini,, S. Chandra Shekar,, A. Srivastava, Chinese J. Catal. 37(2) (2016) 240–249.
[9] Z. Hu,, X. Liu,, D. Meng,, Y. Guo,, Y. Guo,, G. Lu, ACS Catal. 6(4) (2016) 2265–2279.
[10] Q. Ye,, J. Zhao,, F. Huo,, J. Wang,, S. Cheng,, T. Kang,, H. Dai, Catal. Today 175(1) (2011) 603–639.
[11] D. Delimaris,, T. Ioannides, Appl. Catal. B Environ. 89(1) (2009) 295–302.
[12] D. Delimaris,, T. Ioannides, Appl. Catal. B Environ. 84(1) (2008) 303–312.
[13] B. Levasseur,, S. Kaliaguine, Appl. Catal. B Environ. 88(3) (2009) 305–314.
[14] K.C. Soni,, S. Chandra Shekar,, B. Singh,, T. Gopi, J. Colloid Interface Sci. 446 (2015) 226–236.
[15] Q.-F. Deng,, T.-Z. Ren,, B. Agula,, Y. Liu,, Z.-Y. Yuan, J. Ind. Eng. Chem. 20(5) (2014) 3303–3312.
[16] G. Cheng,, L. Yu,, B. Lan,, M. Sun,, T. Lin,, Z. Fu,, X. Su,, M. Qiu,, C. Guo,, B. Xu, Mater. Res. Bull. 75 (2016) 17–24.
[17] T. Lin,, L. Yu,, M. Sun,, G. Cheng,, B. Lan,, Z. Fu, Chem. Eng. J. 286 (2016) 114–121.
[18] H. Sun,, Z. Liu,, S. Chen,, X. Quan, Chem. Eng. J. 270 (2015) 58–65.
[19]T. Lu , F. Su , Q.Zhao , J. Li , C. Zhang , R. Zhang , P. Liu, Separation and Purification Tech., 296 (2022), 121436

[20] L. Li , Q. Yang , D. Wang , Y. Peng , J. Yan , J. Li , J. Crittenden, Chem. Eng.J. Volume 421/2(2021) 127828.
[21] K. Li , C. Chen , H. Zhang , X. Hu , T. Sun , J. Jia, App.Sur. Sci. 496 (2019), 143662
[22] Y. Lyu , C. Li , X. Du , Y. Zhu , Y. Zhang , S. Li, Fuel ,262 (2020), 116610.
[23]X.Zhang , J. Ye , J. Yuan , T. Cai , B. Xiao , Z. Liu , K. Zhao , L.Yang , D. He, Applied Catalysis A: General, 566 (2018) 104-112.
[24] Y. Zheng, Q. Liu, C.P. Shan, Y. Su, K. Fu, S. Lu, R. Han, C. Song, N. Ji, D. Ma, Environ. Sci. Technol. 55 (2021) 5403–5411.
[25] H.C. Genuino,, S. Dharmarathna,, E.C. Njagi,, M.C. Mei,, S.L. Suib, J. Phys. Chem. C 116(22) (2012) 12066–12078.
[26] J. Luo,, Q. Zhang,, J. Garcia-Martinez,, S.L. Suib, J. Am. Chem. Soc. 130(5) (2008) 3198–3207.
[27] J. Hou,, Y. Li,, M. Mao,, L. Ren,, X. Zhao, ACS Appl. Mater. Interfaces 6 (2014) 14981–14987.
[28] S.H. Liang,, F.T.G. Bulgan,, R.L. Zong,, Y.F. Zhu, J. Phys. Chem. C 112 (2008) 5307–5315.
[29] J. Zhang,, Y. Li,, L. Wang,, C. Zhang,, H. He, Catal. Sci. Technol. 5(4) (2015) 2305–2313.
[30] W. Si,, Y. Wang,, Y. Peng,, X. Li,, K. Li,, J. Li, Chem. Commun. 51(81) (2015) 14977–14980.
[31] Y. Liu,, C. Luo,, J. Sun,, H. Li,, Z. Sun,, S. Yan, J. Mater. Chem. A 3 (2015) 5674–5682.
[32] S. Devaraj,, N. Munichandraiah, J. Phys. Chem. C 112(11) (2008) 4406–4417.
[33] N.N. Opembe,, C. Guild,, C. King'Ondu,, N.C. Nelson,, I.I. Slowing,, S.L. Suib, Ind. Eng. Chem. Res. 53(49) (2014) 19044–19051.
[34] X. Wang,, Y. Li, Chem. - A Eur. J. 9(1) (2003) 300–306.
[35] T. Gao,, H. Fjellvåg,, P. Norby, Anal. Chim. Acta 648(2) (2009) 235–239.
[36] P.M. de Wolff, Acta Crystallogr. 12(4) (1959) 341–345.
[37] B. Zhao,, R. Ran,, X. Wu,, D. Weng, Appl. Catal. A Gen. 514 (2016) 24–34.
[38] Y. Du,, L. Wang,, J. Wang,, G. Zheng,, J. Wu,, H. Dai, J. Environ. Sci. 29 (2015) 71–81.
[39] C. Wang,, L. Sun,, Q. Cao,, B. Hu,, Z. Huang,, X. Tang, Appl. Catal. B Environ. 101(3) (2011) 598–605.
[40] K. Selvakumar,, S.M. Senthil Kumar,, R. Thangamuthu,, G. Kruthika,, P. Murugan, Int. J. Hydrogen Energy 39(36) (2014)

21024–21036.
[41] J. Jia,, P. Zhang,, L. Chen, Appl. Catal. B Environ. 189 (2016) 210–218.
[42] M. Piumetti,, D. Fino,, N. Russo, Appl. Catal. B Environ. 163 (2015) 277–287.
[43] Y. Yang,, J. Huang,, S. Wang,, S. Deng,, B. Wang,, G. Yu, Appl. Catal. B Environ. 142–143 (2013) 568–578.
[44] T. Chen,, H. Dou,, X. Li,, X. Tang,, J. Li,, J. Hao, Microporous Mesoporous Mater. 122(1–3) (2009) 270–274.
[45] J. Hou,, Y. Li,, L. Liu,, L. Ren,, X. Zhao, J. Mater. Chem. A 1(23) (2013) 6736.
[46] C. Wang,, J. Ma,, F. Liu,, H. He,, R. Zhang, J. Phys. Chem. C 119(40) (2015) 23119–23126.
[47] H. Einaga,, A. Ogata, J. Hazard. Mater. 164(2–3) (2009) 1236–1241.
[48] M. Sun,, B. Lan,, T. Lin,, G. Cheng,, F. Ye,, L. Yu,, X. Cheng,, X. Zheng, CrystEngComm 15(35) (2013) 7010.
[49] E. Saputra,, S. Muhammad,, H. Sun,, H.M. Ang,, M.O. Tadé,, S. Wang, Appl. Catal. B Environ. 142–143(February) (2013) 729–735.
[50] T. Uematsu,, Y. Miyamoto,, Y. Ogasawara,, K. Suzuki,, K. Yamaguchi,, N. Mizuno, Catal. Sci. Technol. 6(1) (2015) 222–233.
[51] M. Sun, B. Zhang, H. Liu, B. He, F. Ye, L. Yu, C. Sun, H. Wen, RSC Adv. 7(7) (2017) 3958–3965.
[52] T. Gopi,, G. Swetha,, S. Chandra Shekar,, C. Ramakrishna,, B. Saini,, R. Krishna,, P.V.L. Rao, Catal. Commun. 92 (2017) 51–55.

Table-1: Tunnel size, XPS data, specific surface area (m^2/g) and Pore volume (cm^3/g) of MnO_2 catalysts.

Catalyst	Tunnel	Size/Å	XPS Data			BET surface area (m^2/g)	Pore volume (cm^3/g)
			Mn $2p_{3/2}$, Mn^{4+}/Mn^{3+}	Mn 3s AOS	O 1s O_{latt}/O_{ads}		
α-MnO_2	(1 x 1), (2 x 2)	1.89, 4.60	0.94	3.80	1.06	159	0.36
β-MnO_2	(1 x 1)	1.89	1.80	3.97	1.31	83	0.24
γ-MnO_2	(1 x 1), (1 x 2)	1.89, 2.30	0.71	3.69	0.54	119	0.33
δ-MnO_2	interlayer distance	7.00	1.21	3.90	1.61	164	0.42

Table-2: $T_{50\%}$, $T_{90\%}$ for benzene oxidation on MnO_2 catalysts

Catalyst	K^+ atomic wt% [a]	Catalytic Activity (°C)		BET surface area (m^2/g)
		$T_{50\%}$	$T_{90\%}$	
α-MnO_2	6.8	227	264	159
β-MnO_2	-	252	-	83
γ-MnO_2	-	243	276	119
δ-MnO_2	19.7	232	268	164
H-α-MnO_2	3.7	225	261	174
H-δ-MnO_2	2.1	200	238	206

[a]measured by EDS analysis

Figure captions:

Figure 1. X-ray diffraction pattern of α, β, γ and δ-MnO_2 catalysts.

Figure 2: crystal structures of α, β, γ and δ-MnO_2 phases

Figure 3. (a.1), (b.1), (c.1), (d.1) are SEM images of α, β, γ and δ-MnO_2 catalysts. (a.2 to a.4) are TEM images of α-MnO_2 catalyst, (b.2 to b.4) are TEM images of β-MnO_2 catalyst, (c.2 to c.4) are TEM images of γ-MnO_2 catalyst, (d.2 to d.4) are TEM images of δ-MnO_2 catalyst,

Figure 4. H_2-TPR profile of α, β, γ and δ-MnO_2 catalysts.

Figure 5. O_2-TPD profile of α, β, γ and δ-MnO_2 catalysts.

Figure 6. De-convoluted Mn2p3/2 and O1s XPS of α, β, γ and δ-MnO_2 catalysts.

Figure 7. (a) Benzene conversion as a function of temperature, (b) benzene conversion as a function of time of α, β, γ and δ-MnO_2 catalysts.

Figure 8. (a) XRD pattern of H-α and H-δ-MnO_2 catalysts, (b) H_2-TPR pattern of α, δ, H-α and H-δ-MnO_2 catalysts.

Figure 9. TEM images of H-α and H-δ-MnO_2 catalysts.

International Journal of Environmental Sciences
ISSN: 2229-7359
Vol. 11 No. 10s, 2025
https://theaspd.com/index.php

Figure 10. (a) Benzene conversion as a function of temperature, (b) benzene conversion as a function of time of α, δ, H-α and H-δ-MnO_2 catalysts.
Figure 11. (a) TEM and EDS spectra's of H-α-MnO_2 and K-α-MnO_2 catalysts. (b) TEM and EDS spectra's of H-δ-MnO_2 and K-δ-MnO_2 catalysts.

Figure 1.

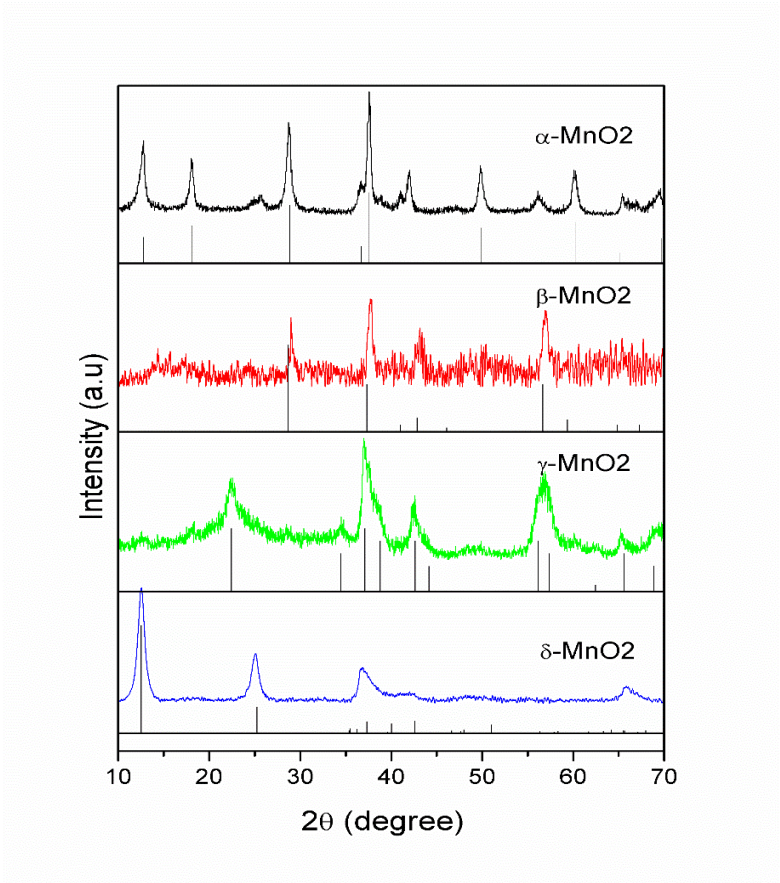

Figure 2.

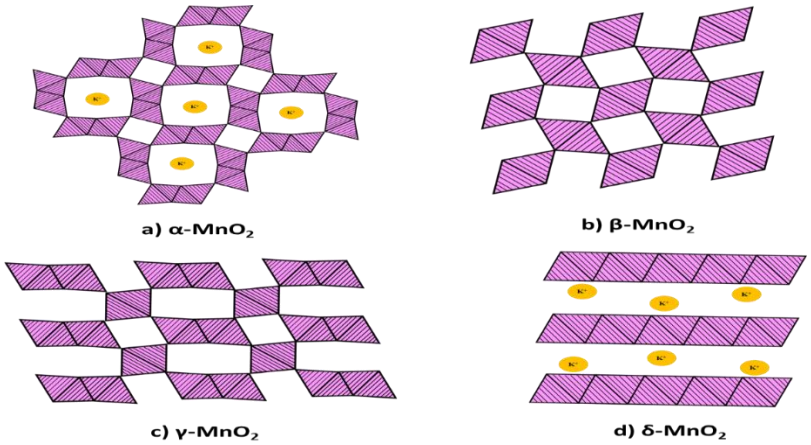

Figure 3.

International Journal of Environmental Sciences
ISSN: 2229-7359
Vol. 11 No. 10s, 2025
https://theaspd.com/index.php

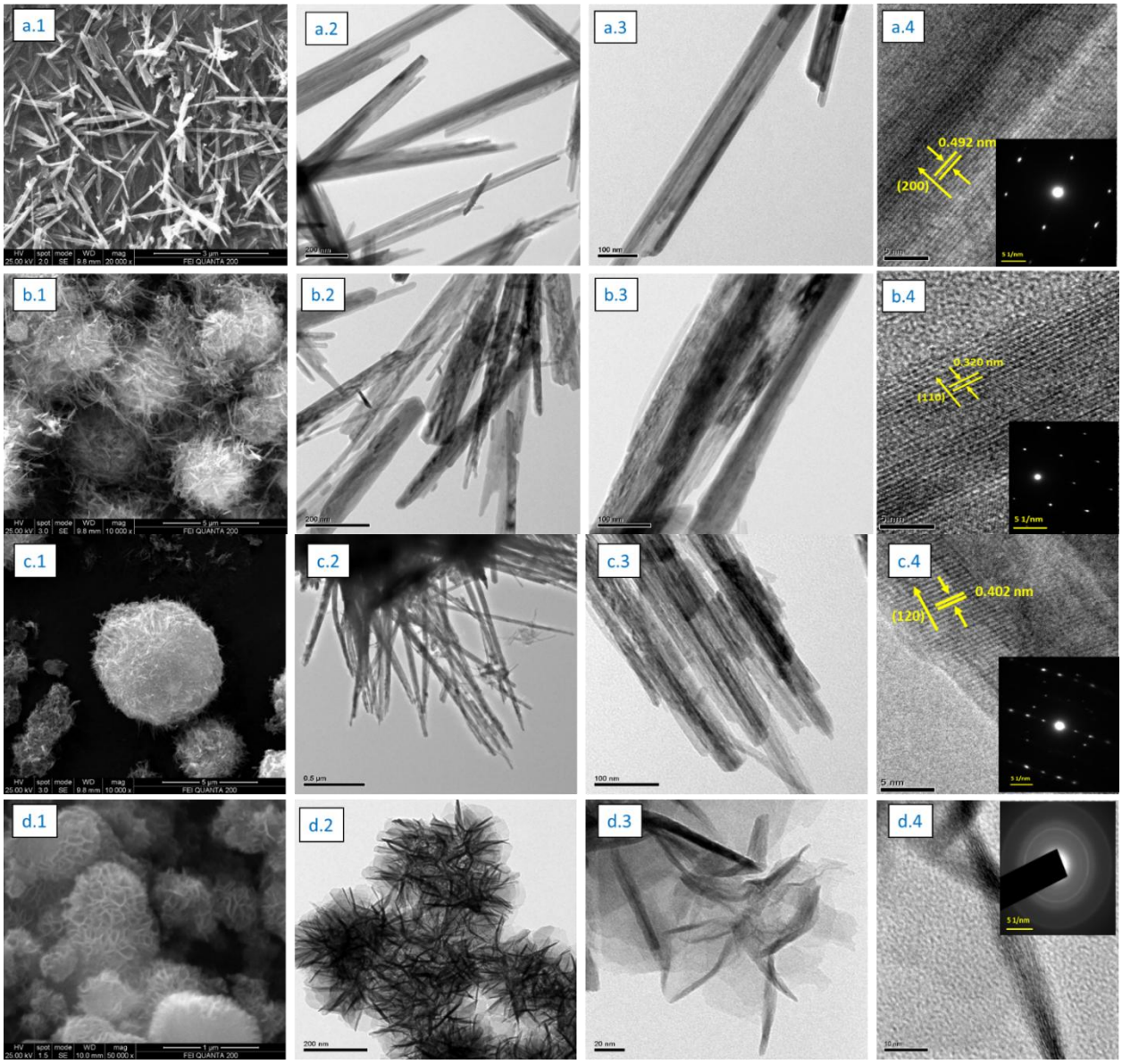

Figure 4.

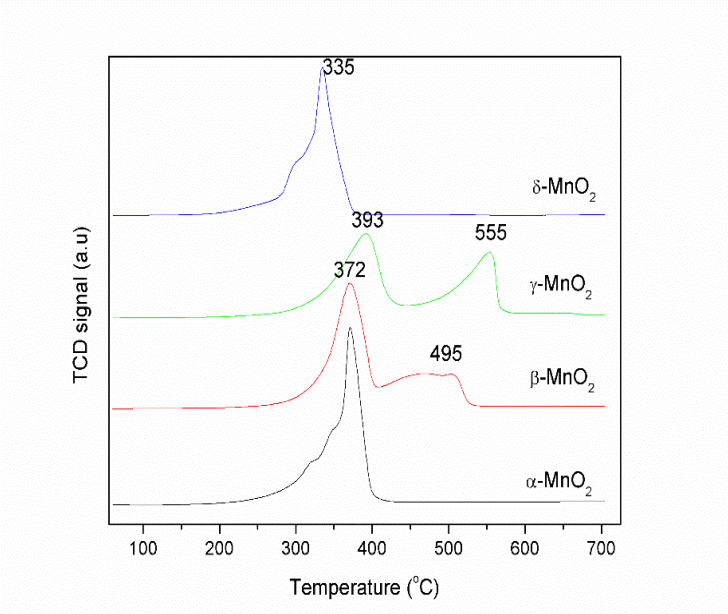

Figure 5.

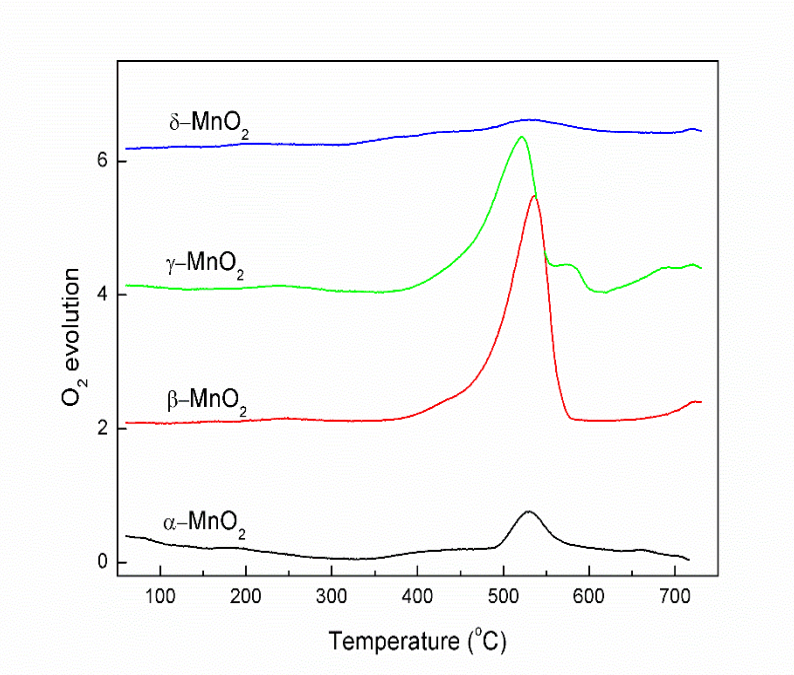

Figure 6.

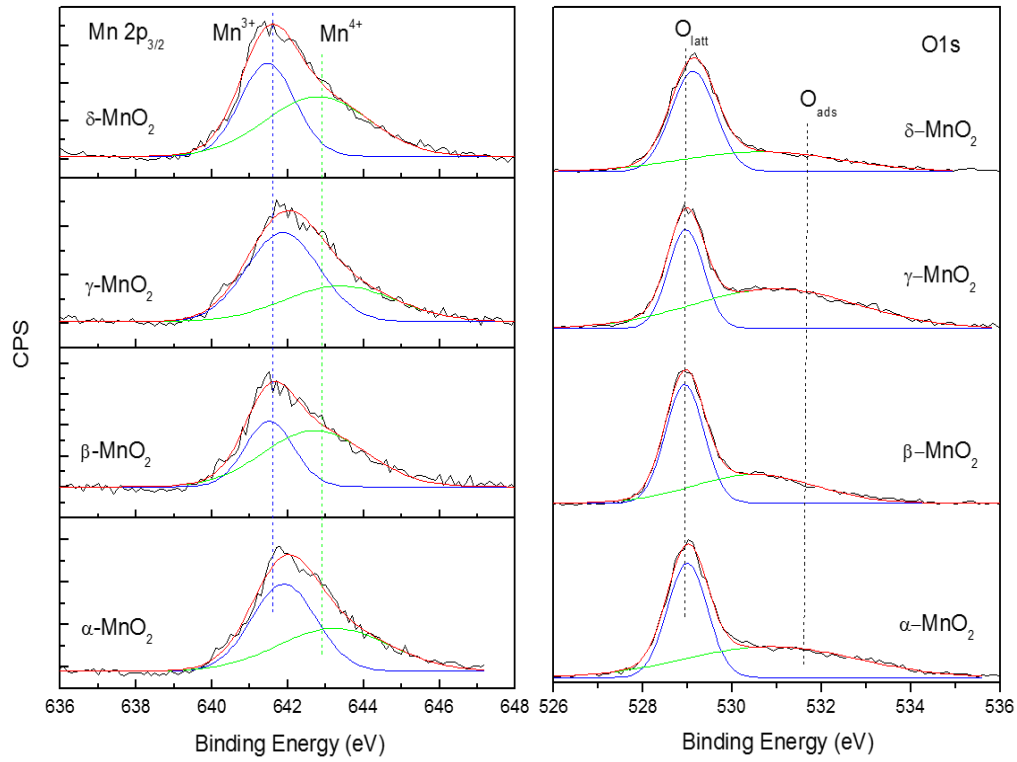

Figure 7.

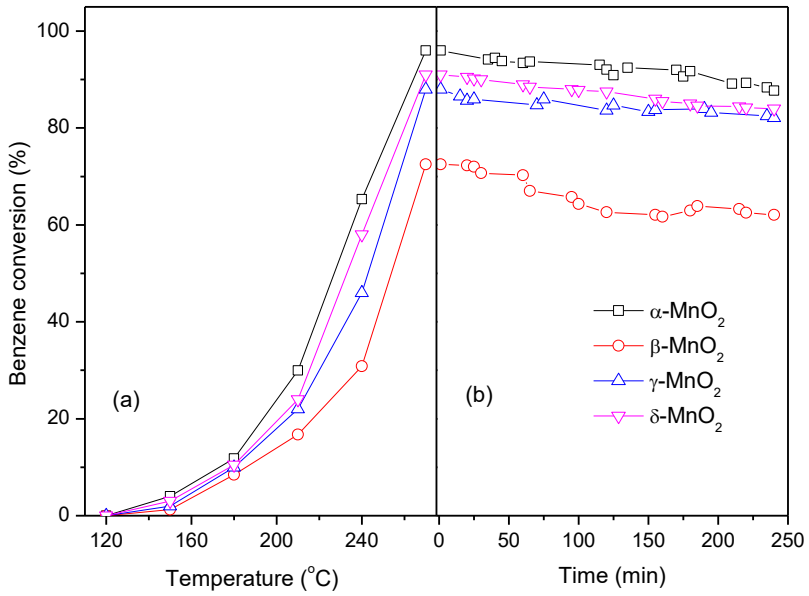

Figure 8.

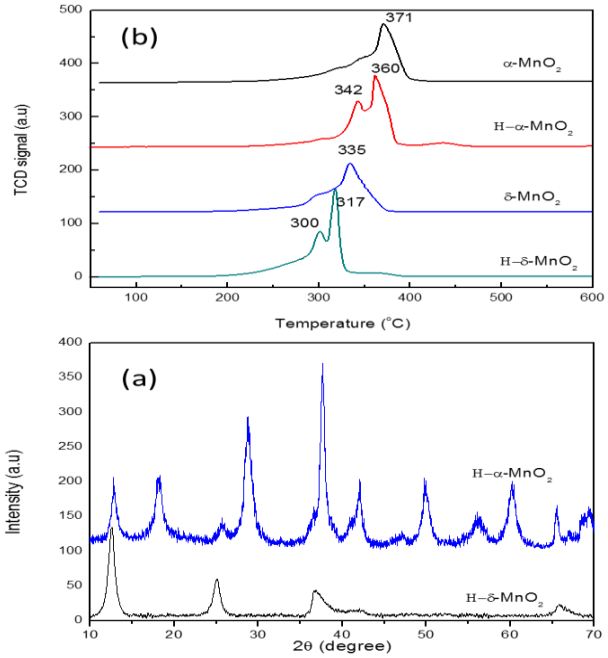

Figure 9.

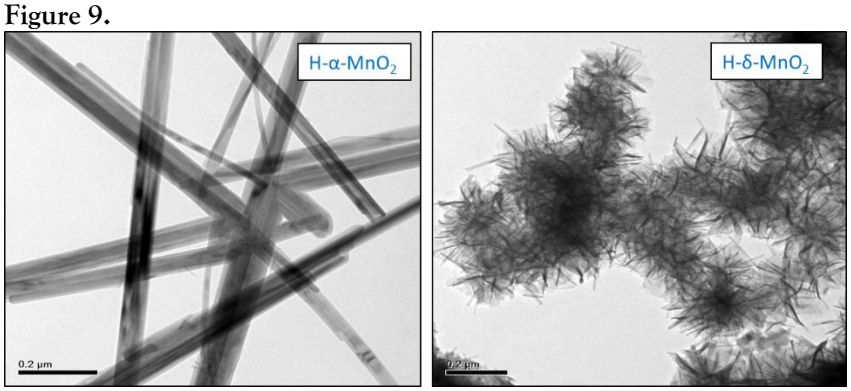

International Journal of Environmental Sciences
ISSN: 2229-7359
Vol. 11 No. 10s, 2025
https://theaspd.com/index.php

Figure 10.

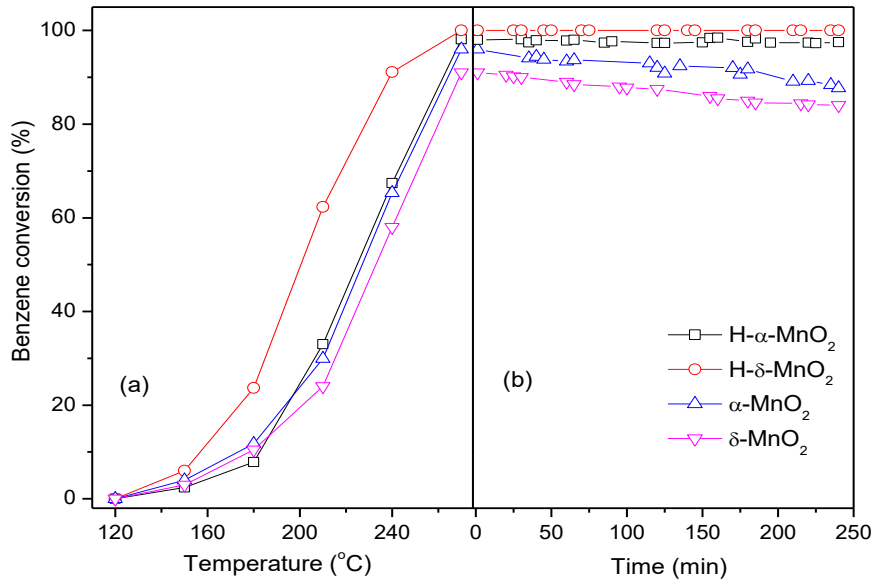

Figure 11(a)

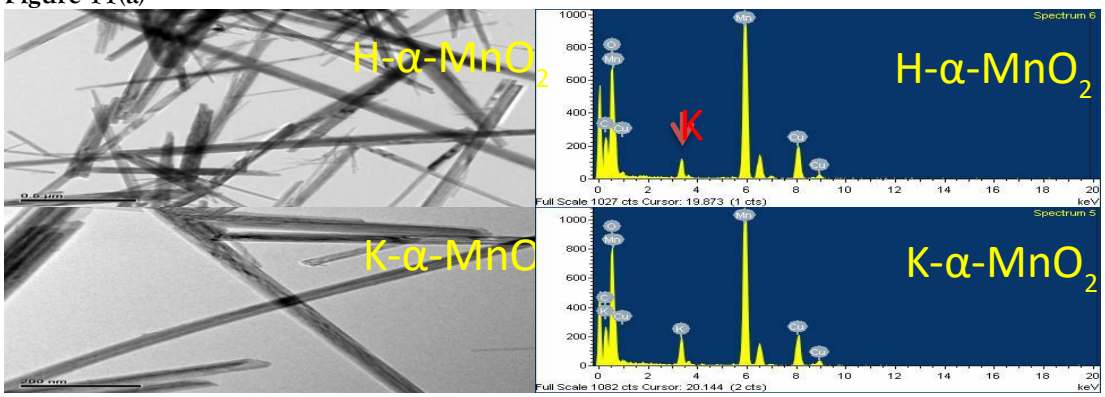

Figure 11(b)